Kramers-Kronig analysis of reflection electron-energy-loss spectra measured with a cylindrical mirror analyzer

Youichi Ohno
Department of Physics, Faculty of General Education, Utsunomiya University, 350 Mine-machi, Utsunomiya, Tochigi 321, Japan
(Received 24 August 1988; revised manuscript received 12 December 1988)

We have discussed a valence-electron energy-loss spectrum measured in reflection geometry using a cylindrical mirror analyzer (CMA) and derived the angular distribution of inelastic scattering, the momentum transfer, and the differential cross section per unit energy. If a critical inelastic-scattering angle is smaller than the angular aperture of the analyzer, the differential cross section no longer depends on momentum transfer. The reflection electron-energy-loss spectroscopy (REELS) spectra of MoS_2 and graphite have been measured and the Kramers-Kronig analysis has been applied. The results are compared with those of the composite energy-loss function calculated from the energy-loss functions perpendicular and parallel to the c axis. It has been shown that the Kramers-Kronig analysis is still valid for the REELS spectra at higher incident energies than 500 eV and that the derived optical constants consist approximately of 80% of the perpendicular component and 20% of the parallel component.

I. INTRODUCTION

Transmission electron-energy-loss spectroscopy (TEELS) in the electron microscope has been exploited as a microanalytical technique.[1,2] It is useful for investigating the energy-loss function, the joint density of states, and some optical constants of a solid in a wide energy range with aid of well-known Kramers-Kronig (KK) relations.[3,4] Reflection electron-energy-loss spectroscopy (REELS) is, on the other hand, commonly used to study surface physics and surface chemistry.[5] Since incidence electrons available in REELS have energies in the range 10–3000 eV and suffer energy losses through a variety of single and collective excitations of free and bound electrons and phonons in a bulk or a surface, the mean free path is small, less than a few decades of Å.[6]

It is known that unlike TEELS several important but difficult problems are raised in REELS. As incident energy approaches the ionization threshold, optically forbidden transitions are possible through exchange interaction between an incident electron and a valence or a conduction electron in a solid[7] and through large momentum transfer in the inelastic-scattering process.[8,9] The momentum transfer also causes wave-vector-dependent transitions in the excitation of valence and conduction electrons.[10] In addition, we can observe the incident-energy dependence of a REELS spectrum that results from different mean free paths.[11] These phenomena allow the unique information of electronic structures of atoms, molecules, and solids, but they complicate the interpretation of a REELS spectrum as compared with that of a TEELS spectrum.

In most of the REELS studies up to date,[12–14] our attention has focused on peak positions and the energy shifts arising from the variations of surface conditions and incident energy. Then, the spectra are commonly obtained in the second-derivative form using a lock-in amplifier so as to avoid a large background. Recently, however, they can be easily obtained in the pulse-counting mode with a cylindrical mirror analyzer (CMA) and a hemispherical sector analyzer (HSA) to take the energy-distribution curve directly. If the KK analysis is valid for a REELS spectrum as well as a TEELS spectrum, the following merits are considered.

(1) Sample preparation is easy. We do not require a thin-film form for a sample investigated.
(2) Highly resolved spectra can be easily obtained because the incident energy is much smaller than that in TEELS.
(3) Crystal defects and charging effects which are caused by electron bombardment during the measurements are reduced.

In spite of the merits, few attempts of the KK analysis have been made because derivation of the energy-loss function is not well understood. In other words, we have no full knowledge of the inelastic-scattering process in reflection geometry, especially for the angular distribution of inelastic scattering, the momentum transfer, and the differential cross section per unit energy.

In the present study we have attempted to establish the theoretical foundation of the inelastic-scattering process at normal incidence, shown in Fig. 1, and to test the validity of the KK analysis. In Sec. II we discuss the inelastic-scattering process in which the CMA is employed as an analyzer and derive the angular distribution of inelastic scattering, the momentum transfer, and the differential cross section per unit energy. The measured intensity is then correlated with the energy-loss functions perpendicular and parallel to the c axis. In Sec. III the experimental procedures of REELS measurements and the KK analysis are presented. In Sec. IV the results ob-

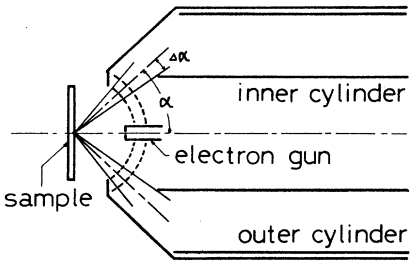

FIG. 1. Arrangement for REELS measurements when using a CMA, which is equipped with a coaxial electron gun and two spherical retarding grids. The incident angle α and the angular aperture $\Delta\alpha$ of the CMA are 42.3° and 6°, respectively. Electron beams impinge perpendicularly on a surface.

tained for MoS_2 and graphite are discussed and compared with those of the composite energy-loss function derived from the energy-loss functions perpendicular and parallel to the c axis.

II. THEORY

REELS studies to date[15,16] have indicated that inelastic scattering for excitation of valence and conduction electrons occurs dominantly at small angles, accompanied with large elastic collision. The process is illustrated schematically in Fig. 2, in which incident electrons impinge perpendicularly on a surface and travel in a bulk, suffering energy losses until they reflect from the surface. For simplicity, we now consider the single inelastic-scattering process followed or preceded by large elastic collision. O and O' denote inelastic events before and after elastic collision, respectively, and P represents an elastic event. Due to energy- and momentum-conservation rules, the following relations holds,

$$E_p = E' + \Delta E \tag{1}$$

and

$$\mathbf{k}_0 = \mathbf{k}' + \mathbf{q} , \tag{2}$$

where E_p, E', $\mathbf{k}_0$, and $\mathbf{k}'$ are the energies and the wave vectors of an incident electron before and after inelastic scattering, respectively, ΔE is the energy loss, and $\mathbf{q}$ is the momentum transfer. In the free-electron model the magnitude of the momentum transfer is then given by

$$q = \sqrt{2}k_0[(1-\theta_e)-(1-2\theta_e)^{1/2}\cos\theta]^{1/2} , \tag{3a}$$

where

$$k_0 = \frac{(2mE_p)^{1/2}}{\hbar} \quad \text{and} \quad \theta_e = \frac{\Delta E}{2E_p} .$$

Here, $\hbar$ is Planck's constant divided by 2π, m is the mass of a free electron, and θ is the inelastic-scattering angle. At normal incidence the parallel and perpendicular components of the momentum transfer with respect to the c axis are, respectively, given by

$$q_\parallel = k_0[1-(1-2\theta_e)^{1/2}\cos\theta] \approx k_0\theta_e \tag{3b}$$

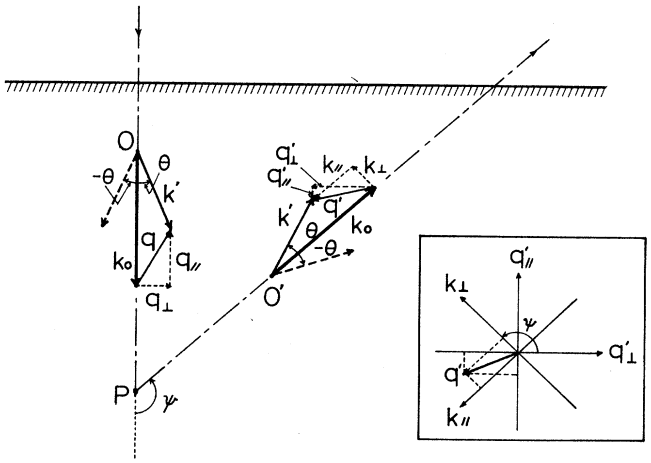

FIG. 2. Schematic diagram for the reflection electron energy-loss process. O and O' denote the inelastic events before and after elastic collision, respectively. P denotes the elastic collision. $\mathbf{k}$ and $\mathbf{k}'$ are the wave vectors of an incident electron and an inelastically scattered electron, respectively. $\mathbf{q}$ is the momentum transfer. ψ and θ are the elastic- and inelastic-scattering angles, respectively. The total scattering angle is about 137.7°, which is determined by the incidence angle and the angular aperture of the CMA. $q_\perp$, $q_\parallel$, $q'_\perp$, and $q'_\parallel$ are the perpendicular and parallel components of the momentum transfers with respect to the c axis before and after elastic collision, respectively. $k_\perp$ and $k_\parallel$ are the perpendicular and parallel components of the momentum transfer with respect to the beam direction, respectively.

and

$$q_\perp = k_0(1-2\theta_e)^{1/2}\sin\theta \approx k_0\theta . \tag{3c}$$

The right-hand equalities in (3b) and (3c) are satisfied only when $\theta_e \ll 1$ and θ is so small that one may assume that $\sin\theta \approx \theta$. In that case Eq. (3a) is approximated as follows:

$$q^2 \approx k_0^2(\theta^2+\theta_e^2). \tag{3d}$$

According to the Bethe theory, the differential cross section for inelastic scattering per unit energy and per unit solid angle is written within the single-electron model and the first Born approximation by[17]

$$\frac{\partial^2\sigma}{\partial\Omega\,\partial E} = \frac{4}{a_0^2q^4}\sum_f \left|\left\langle f\left|\sum_{r_j}\exp(i\mathbf{q}\cdot\mathbf{r}_j)\right|i\right\rangle\right|^2 \times\delta(E_f-E_i-\Delta E) , \tag{4}$$

where a_0 is the Bohr radius, $\mathbf{r}_j$ is the position vector of the electron participating in the transition, and $|i\rangle$ and $|f\rangle$ are the initial and the final states with energy E_i and E_f, respectively. If $\mathbf{q}\cdot\mathbf{r}_j \ll 1$, dipole selection rules hold and the differential cross section is given by

$$\frac{\partial^2\sigma}{\partial\Omega\,\partial E} = \frac{4}{a_0^2q^4}(q_\perp^2|M_\perp|^2+q_\parallel^2|M_\parallel|^2) , \tag{5}$$

where $|M_\perp|^2$ and $|M_\parallel|^2$ are the matrix elements perpen-

dicular and parallel to the c axis, respectively, and are written

$$|M_\perp|^2=\sum_f \sum_{r_j} |\langle f|r_{j\perp}|i\rangle|^2 \delta(E_f-E_i-\Delta E) \tag{6a}$$

and

$$|M_\parallel|^2=\sum_f \sum_{r_j} |\langle f|r_{j\parallel}|i\rangle|^2 \delta(E_f-E_i-\Delta E) . \tag{6b}$$

Here, $r_{j\perp}$ and $r_{j\parallel}$ are the perpendicular and parallel components of the position vector of a j electron, respectively. As a solid angle is written by

$$d\Omega=2\pi \sin\theta\, d\theta \approx 2\pi\theta\, d\theta=\frac{2\pi}{k_0^2} q_\perp\, dq_\perp , \tag{7}$$

the differential cross section per unit energy and per unit scattering angle is then given by

$$\left|\frac{\partial^2\sigma}{\partial\theta\,\partial E}\right|=\frac{8\pi}{a_0^2k_0^2}\frac{|\theta|}{(\theta^2+\theta_e^2)^2}(\theta^2|M_\perp|^2+\theta_e^2|M_\parallel|^2) . \tag{8a}$$

If a sample investigated is isotropic, $|M_\perp|^2=|M_\parallel|^2=|M|^2$ and then

$$\left|\frac{\partial^2\sigma}{\partial\theta\,\partial E}\right|=\frac{8\pi}{a_0^2k_0^2} f(\theta)|M|^2 , \tag{8b}$$

where

$$f(\theta)=\frac{|\theta|}{\theta^2+\theta_e^2}=\frac{1}{\theta_e}\frac{|X|}{1+X^2} \tag{9}$$

and

$$X=\theta/\theta_e \approx q_\perp/q_\parallel .$$

$f(\theta)$ is a function which has a maximum value at $X=1$ and approaches $1/\theta_e|X|$ at large X. Figure 3 shows the angular distribution of inelastic-scattering events, which is plotted as $2\theta_e f(X)$. It is found that if θ_e is less than 0.02, inelastic scattering occurs dominantly at small angle and then the assumptions in deriving Eq. (8a) are valid. In several cases the values of θ_e are tabulated in Table I. For the valence-electron energy-loss spectra up to 20 eV, the above condition is satisfied for incident energies higher than 500 eV. Thus we may conclude that small-angle inelastic-scattering events dominantly contribute to the spectra as confirmed by up to date studies.[15,16] It is worth noting that the differential cross section should be represented as a function of X rather than θ.

Next, we will derive the differential cross section per unit energy. For this purpose, we first assume the existence of the critical X value which gives a criterion that

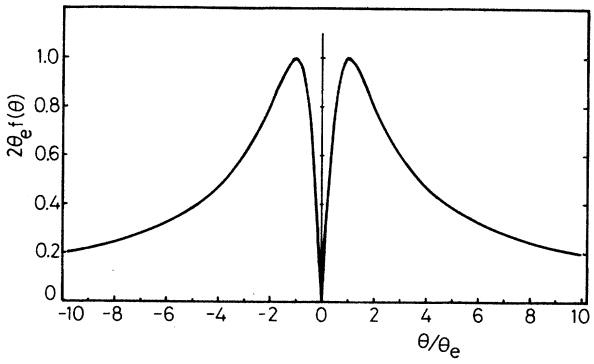

FIG. 3. Angular distribution of inelastic-scattering events. The vertical axis is multiplied by $2\theta_e$, while the horizontal axis is divided by θ_e.

we may regard the contribution to the differential cross section as negligibly small or large. When it is denoted by X_c, the corresponding critical inelastic-scattering angle θ_c and the perpendicular component of the critical momentum transfer, $q_{\perp c}$, are defined by the equations

$$X_c=\theta_c/\theta_e=q_{\perp c}/q_\parallel . \tag{10}$$

The differential cross section per unit energy is then given, from Eqs. (5) and (7), by

$$\begin{aligned}\frac{d\sigma}{dE}&=\int_0^{q_{\perp c}}\frac{8\pi q_\perp dq_\perp}{a_0^2k_0^2q^4}(q_\perp^2|M_\perp|^2+q_\parallel^2|M_\parallel|^2)\\&=\frac{4\pi}{a_0^2k_0^2}\left[\left[\ln|1+X_c^2|-\frac{X_c^2}{1+X_c^2}\right]|M_\perp|^2+\frac{X_c^2}{1+X_c^2}|M_\parallel|^2\right] .\end{aligned} \tag{11}$$

In deriving Eq. (11), we have assumed that the matrix elements $|M_\perp|^2$ and $|M_\parallel|^2$ are independent of q. This assumption is reasonable at small q.

The above considerations are valid for the inelastic-scattering process before elastic collision, but for the inelastic-scattering process after elastic collision some modifications are required. After elastic collision the perpendicular and parallel components of the momentum transfer with respect to the c axis are given by

$$\begin{aligned}\begin{bmatrix}q'_\perp\\q'_\parallel\end{bmatrix}&=\begin{bmatrix}\cos\psi & -\sin\psi\\ \sin\psi & \cos\psi\end{bmatrix}\begin{bmatrix}q_\perp\\q_\parallel\end{bmatrix}\\&=\begin{bmatrix}\cos\psi & -\sin\psi\\ \sin\psi & \cos\psi\end{bmatrix}\begin{bmatrix}k_\perp\\k_\parallel\end{bmatrix} ,\end{aligned} \tag{12}$$

TABLE I. $\theta_e(\Delta E/2E_p)$ in several cases. E_p and ΔE (both in eV) are incident energy and energy loss, respectively.

	$E_p=200$	$E_p=500$	$E_p=1000$	$E_p=2000$
$\Delta E=2$	0.005	0.002	0.001	0.0005
$\Delta E=10$	0.025	0.01	0.005	0.0025
$\Delta E=20$	0.05	0.02	0.01	0.005

where ψ is the elastic-scattering angle and $k_\perp$ and $k_\parallel$ are, respectively, the perpendicular and parallel components of the momentum transfer with respect to the beam direction and are given by

$$k_\perp \approx k_0\theta \tag{13a}$$

and

$$k_\parallel \approx k_0\theta_e \ . \tag{13b}$$

For the CMA, Eq. (12) is simplified by substituting 135° for ψ; that is,

$$\begin{bmatrix} q'_\perp \\ q'_\parallel \end{bmatrix} = \frac{\sqrt{2}}{2}\begin{bmatrix} -1 & -1 \\ 1 & -1 \end{bmatrix}\begin{bmatrix} k_\perp \\ k_\parallel \end{bmatrix} . \tag{12'}$$

In this case the total momentum transfer and the solid angle are, respectively, given by

$$(q')^2 = k_\perp^2 + k_\parallel^2 \tag{14}$$

and

$$d\Omega' = 2\pi\theta\, d\theta = \frac{2\pi}{k_0^2}k_\perp dk_\perp \ . \tag{15}$$

On the other hand, the differential cross section per unit energy and per unit solid angle is given in the same manner as Eq. (5); that is,

$$\frac{\partial^2\sigma'}{\partial\Omega'\,\partial E} = \frac{4}{a_0^2(q')^4}[(q'_\perp)^2|M_\perp|^2 + (q'_\parallel)^2|M_\parallel|^2] , \tag{16}$$

and the differential cross section per unit energy is given by

$$\frac{d\sigma'}{dE} = \int_0^{k_{\perp c}} dk_\perp \frac{8\pi k_\perp}{a_0^2k_0^2(q')^4}\left[\frac{(k_\perp+k_\parallel)^2}{2}|M_\perp|^2 + \frac{(k_\perp-k_\parallel)^2}{2}|M_\parallel|^2\right]$$

$$= \frac{4\pi}{a_0^2k_0^2}\left[\left[\tfrac{1}{2}\ln|1+X_c^2| - \frac{X_c}{1+X_c^2} + \tan^{-1}X_c\right]|M_\perp|^2 + \left[\tfrac{1}{2}\ln|1+X_c^2| + \frac{X_c}{1+X_c^2} - \tan^{-1}X_c\right]|M_\parallel|^2\right] , \tag{17}$$

where

$$X_c = \theta_c/\theta_e = k_{\perp c}/k_\parallel \ .$$

Consequently, as the incident beam flux is I_0 and the probing depth is D, the measured intensity of the REELS spectrum is given by

$$I_0\left[D\frac{d\sigma}{dE} + \left|\frac{D}{\cos\psi}\right|\frac{d\sigma'}{dE}\right] = \frac{4\pi I_0 D}{a_0^2k_0^2}\left[\left[\frac{2+\sqrt{2}}{2}\ln|1+X_c^2| - \frac{X_c(X_c+\sqrt{2})}{1+X_c^2} + \sqrt{2}\tan^{-1}X_c\right]|M_\perp|^2\right.$$

$$\left. + \left[\frac{\sqrt{2}}{2}\ln|1+X_c^2| + \frac{X_c(X_c+\sqrt{2})}{1+X_c^2} - \sqrt{2}\tan^{-1}X_c\right]|M_\parallel|^2\right] . \tag{18}$$

Since the energy-loss functions perpendicular and parallel to the c axis are, respectively, written within the dipole approximation by

$$\mathrm{Im}(-1/\epsilon_\perp) = 4\pi^2ne^2|M_\perp|^2 \tag{19a}$$

and

$$\mathrm{Im}(-1/\epsilon_\parallel) = 4\pi^2ne^2|M_\parallel|^2 , \tag{19b}$$

then the mixing ratio of the perpendicular to the parallel component is given by

$$R = \frac{[(2+\sqrt{2})/2]\ln|1+X_c^2| - [X_c(X_c+\sqrt{2})]/(1+X_c^2) + \sqrt{2}\tan^{-1}X_c}{(\sqrt{2}/2)\ln|1+X_c^2| + [X_c(X_c+\sqrt{2})]/(1+X_c^2) - \sqrt{2}\tan^{-1}X_c}\,\frac{\mathrm{Im}(-1/\epsilon_\perp)}{\mathrm{Im}(-1/\epsilon_\parallel)} . \tag{20}$$

If we may substitute 10 for X_c in Eq. (18), the energy-loss function is of the form

$$\mathrm{Im}[-1/\epsilon(E)] \approx 0.8\,\mathrm{Im}[-1/\epsilon_\perp(E)] + 0.2\,\mathrm{Im}[-1/\epsilon_\parallel(E)] . \tag{21}$$

Thus we may suggest that the energy-loss function derived from the REELS spectrum contains 80% of the perpendicular component and 20% of the parallel component. If the sample is isotropic, the measured intensity is proportional to

$$\frac{4\pi I_0 D}{a_0^2k_0^2}(1+\sqrt{2})\ln|1+X_c^2|\,|M|^2 = \frac{(1+\sqrt{2})I_0D}{\pi a_0^2ne^2k_0^2}\ln|1+X_c^2|\,\mathrm{Im}(-1/\epsilon) . \tag{22}$$

It is found that the last equation is quite similar to that of TEELS where X_c is replaced by X_α ($=\Delta\alpha/\theta_e$).[2] If the

angular aperture of the analyzer, $\Delta\alpha$, is too small to define the critical inelastic-scattering angle, X_c should be replaced by X_α for inelastic scattering after elastic collision. In that case Eqs. (18), (20), and (21) are the functions of θ_e, so that the measured intensity and mixing ratio depend on incident energy and energy loss. The results are shown in Figs. 4(a) and 4(b). However, if $\Delta\alpha$ is large enough to define θ_c, X_c is a constant independent of incident energy and energy loss. As a result, R is unchanged and the measured intensity is directly correlated to the energy-loss function. The above condition would be fulfilled by using the analyzer with large angular aperture. Consequently, when using the CMA, which has a relatively large angular aperture, we require no angular corrections in making the KK analysis. This result is important because in TEELS experiments we commonly require angular corrections.

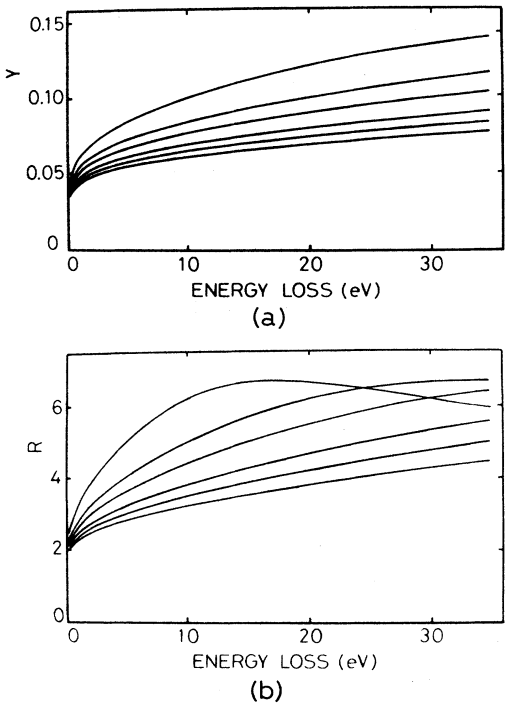

FIG. 4. (a) Angular correction for measured intensities and (b) the mixing ratio of the perpendicular energy-loss function to the parallel one. The calculations have been carried out in the case that the upper limit of integral in Eq. (17) is determined by the angular aperture of the CMA and that a sample investigated is isotropic. The angular correction is then given by

$$Y=\frac{1}{\ln|1+X_c^2|+\sqrt{2}\ln|1+X_\alpha|^2}$$

and the mixing ratio is

$$R=\frac{\ln|1+X_c^2|-\frac{X_c^2}{1+X_c^2}+\frac{\sqrt{2}}{2}\ln|1+X_\alpha|^2-\frac{\sqrt{2}X_\alpha}{1+X_\alpha^2}+\sqrt{2}\tan^{-1}X_\alpha}{\frac{X_c^2}{1+X_c^2}+\frac{\sqrt{2}}{2}\ln|1+X_\alpha^2|+\frac{\sqrt{2}X_\alpha}{1+X_\alpha^2}-\sqrt{2}\tan^{-1}X_\alpha}$$

where $X_c=20$ and $X_\alpha=\Delta\alpha/\theta_e=2\Delta\alpha E_p/\Delta E$. The parameter is incident energy, which is 200, 400, 600, 1000, and 2000 eV going from the top to the bottom.

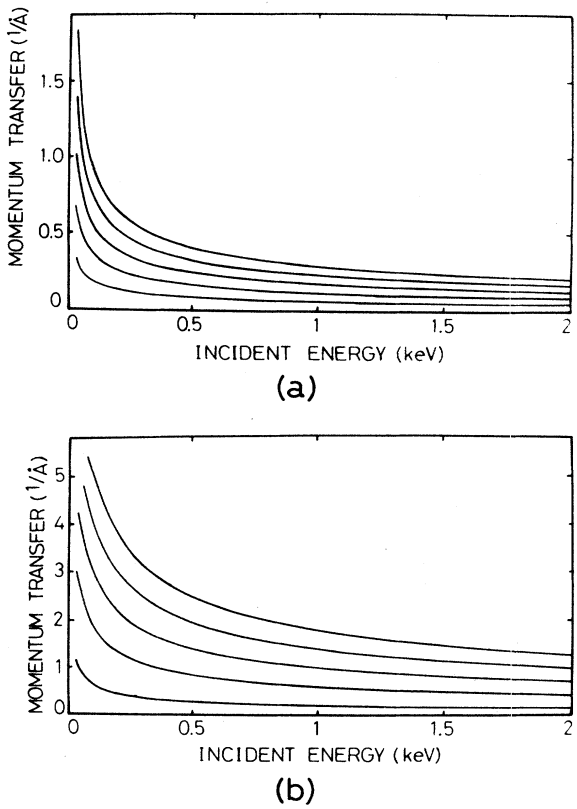

FIG. 5. Momentum transfers at (a) $\theta=\theta_e$ and (b) $\theta=10\theta_e$. The parameter is energy loss, which is 5, 10, 15, 20, and 25 eV going from the bottom to the top.

For inelastic scattering at $\theta=\theta_e$, the momentum transfer monotonously decreases with E_p and the dipole approximation is valid at least for the incident energies higher than 500 eV, whereas for inelastic scattering at $\theta=10\theta_e$ the momentum transfer also decreases, but the dipole approximation is no longer valid in the wide energy region (see Fig. 5). At $\theta=0.1$ rad, which corresponds to the angular aperture of the CMA, the momentum transfer increases and the dipole approximation is not valid. Experimental results, on the other hand, suggest that the valence-electron–excitation REELS spectrum is determined mainly by inelastic scattering near θ_e, and the dipole approximation is still valid at E_p values of more than 500 eV, as discussed below.

III. EXPERIMENTS

In REELS spectra of real surfaces we encounter many difficulties and complexities, such as creation of localized surface states due to dangling bonds and interactions between surface atoms and foreign atoms and molecules, which are different from sample to sample under different experimental conditions. Since the main purpose of the

present study is to clarify the basic information involved in a REELS spectrum under particular conditions and to verify the validity of the KK analysis, we have made an effort to treat an ideal surface, so far as circumstances permit, to avoid any difficulties. The nearly ideal surface that is made by crossing an infinite crystal with a plane is experimentally available by use of layered materials such as MoS_2 and graphite. Then, the valence-electron energy-loss spectra of MoS_2 and graphite have been measured in reflection geometry using the CMA. The single crystals of MoS_2 are prepared by chemical-vapor reaction in an evacuated and then closed silica ampoule, while the samples of highly oriented pyrolytic graphite (HOPG) are from the Union Carbide Co. These crystals are constructed by stacking layers which are weakly bonded with each other by van der Waals force, so that atomically clean and smooth surfaces are easily prepared by cleaving with adhesive tape in the atmosphere just before the measurements. The resulting surfaces, which are perpendicular to the c axis, are quite inactive for foreign atoms and molecules. Auger-electron-spectroscopy (AES) analysis displays a small amount of carbon contamination, but no other contamination is detected, even after long-time measurements.

REELS measurements have been carried out in the pulse-counting mode using the double-pass CMA with retarding grids (PHI model no. 15-255G) as shown in Fig. 1. The pass energy of the CMA is 25 eV, giving a spectral resolution of about 0.8 eV. The details of our experimental apparatus and data acquisition and processing system have been described in previous papers.[18,19] Pulse-counting data are stored in the disk drive unit of a personal computer (NEC PC 9801F3). Afterwards, they are utilized to derive the energy-loss function and some optical constants.

The energy-loss function is derived from a measured spectrum using the Bethe f sum rule, which is written[2]

$$n_{\text{eff}}=a\int_0^E E'\,\text{Im}[-1/\epsilon(E')]dE' \tag{23}$$

and

$$a=\frac{2\epsilon_0 m}{\pi\hbar^2 e^2 n}\ , \tag{24}$$

where n_{eff} is the effective number of electrons contributing to the energy losses and n is the number of atoms or molecules per unit volume. When the critical inelastic-scattering angle θ_c or X_c is defined, the normalized intensity $I(E)$ of a REELS spectrum is directly proportional to the energy-loss function as discussed above and is written by

$$I(E)=B\,\text{Im}[-1/\epsilon(E)]\ , \tag{25}$$

where B is a constant independent of energy E. Then the energy-loss function is derived using the relation

$$\text{Im}[-1/\epsilon(E)]=\frac{n_{\text{eff}}I(E)}{a\int_0^E E'I(E')dE'}\ . \tag{26}$$

Since surface contribution to a REELS spectrum decreases with increasing incident energy, we can separate it by measuring the spectra at various incident energies. At $E_p=2000$ eV or higher incident energies, the bulk contribution is dominant. However, if surface losses cannot be completely removed, we should introduce a parameter k $(0<k<1)$ into the constant a so as to give the correct $\epsilon_1(0)$ value.

The application of the KK relation to the derived energy-loss function gives the real part of $1/\epsilon(E)$;[20] that is,

$$\text{Re}[1/\epsilon(E)]=1-\frac{2}{\pi}\text{P}\int_0^\infty \text{Im}[-1/(E')]\frac{E'}{(E')^2-E^2}dE'\ , \tag{27}$$

where P denotes the Cauchy principal part of the integral. The KK transform has been carried out by taking a sine transform of the energy-loss function, followed by the inverse cosine transform. These calculations have been done using a fast Fourier algorithm, in which the higher-energy tail of a plasmon peak is extrapolated to zero at the higher-energy end of a Fourier-transform range in order to avoid the contribution of higher-order peaks. The complex dielectric function is then given by

$$\begin{aligned}\epsilon(E)&=\epsilon_1(E)+i\epsilon_2(E)\\&=\frac{\text{Re}[1/\epsilon(E)]+i\,\text{Im}[-1/\epsilon(E)]}{\{\text{Re}[1/\epsilon(E)]\}^2+\{\text{Im}[-1/\epsilon(E)]\}^2}\ ,\end{aligned} \tag{28}$$

where $\epsilon_1(E)$ and $\epsilon_2(E)$ are the real and imaginary parts of the dielectric constant, respectively. Once the quantities are evaluated, the refractive index $n(E)$, the extinction coefficient $k(E)$, and the reflectivity $R(E)$ are computed using the following relations:

$$n(E)=(\tfrac{1}{2}\{[\epsilon_1(E)]^2+[\epsilon_2(E)]^2\}^{1/2}+\epsilon_1(E))^{1/2}\ , \tag{29}$$

$$k(E)=(\tfrac{1}{2}\{[\epsilon_1(E)]^2+[\epsilon_2(E)]^2\}^{1/2}-\epsilon_1(E))^{1/2}\ , \tag{30}$$

$$R(E)=\frac{[n(E)-1]^2+[k(E)]^2}{[n(E)+1]^2+[k(E)]^2}\ . \tag{31}$$

Since surface losses are contained in the measured spectra and the loss function is derived from the real and imaginary parts of the complex dielectric constant by the equation

$$\text{Im}\{-1/[\epsilon(E)+1]\}=\frac{\epsilon_2(E)}{[\epsilon_1(E)+1]^2+[\epsilon_2(E)]^2}\ , \tag{32}$$

the KK analysis is, in practice, repeatedly carried out in order to isolate the surface losses from the bulk ones. Our computer program for the KK analysis is referred to that of Egerton.[2]

IV. RESULTS AND DISCUSSION

Figures 6 and 7 show the energy-distribution curves of the electrons emitted or reflected from the cleaved surfaces of MoS_2 and graphite. A large peak appears near the threshold, which arises from secondary-electron emission. Auger peaks such as sulfur LVV and carbon KVV peaks appear in the intermediate-energy region and energy-loss structures due to excitation of valence elec-

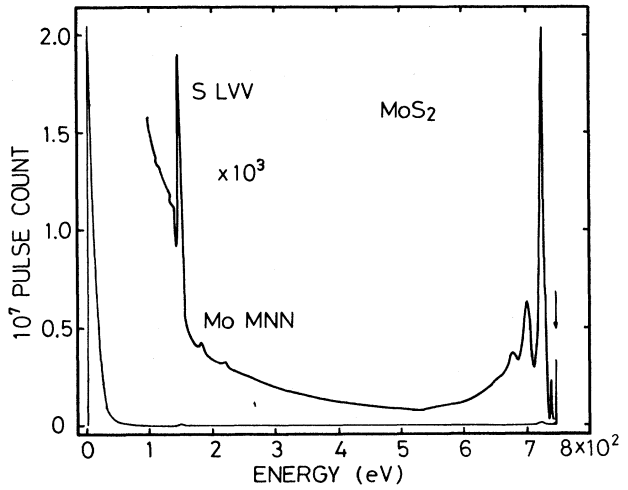

FIG. 6. Electron-energy-distribution curve of MoS_2.

trons appear just below the elastic peak which is denoted by an arrow. As can be seen from the figures, secondary-electron emission affects the energy-loss structures as well as the Auger peaks as a smoothly varying background. A background like this is more significant in REELS than in TEELS, especially in the cases of metallic materials and lower incident energy. Then, it must be subtracted by appropriate methods to isolate the energy-loss structures. It is also found that doubly and triply excited plasmon peaks are observed in REELS spectra as well as in TEELS spectra. Such a multiple-scattering effect is also subtracted to derive the energy-loss function. For this purpose, the Fourier-logarithmic deconvolution and the Fourier-ratio methods have been developed by Johnson and Spence,[21] Leapman and Swyt,[22] and Egerton and Whelan.[23] They are summarized in Ref. 2.

Figure 8 shows the REELS spectrum of MoS_2 together with the energy-loss functions perpendicular and parallel to the c axis (middle and bottom solid lines) obtained

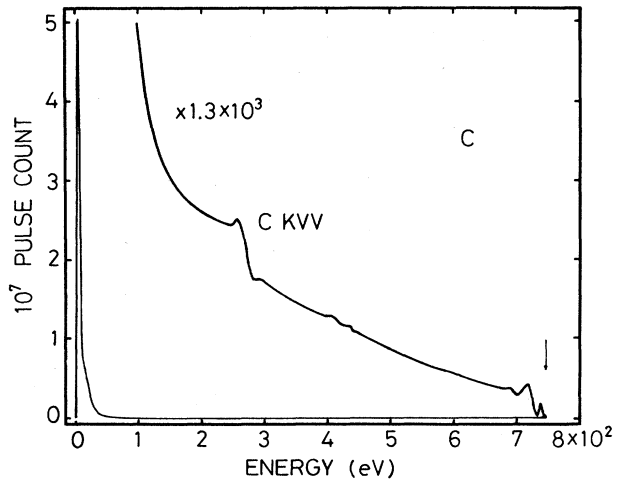

FIG. 7. Electron-energy-distribution curve of graphite.

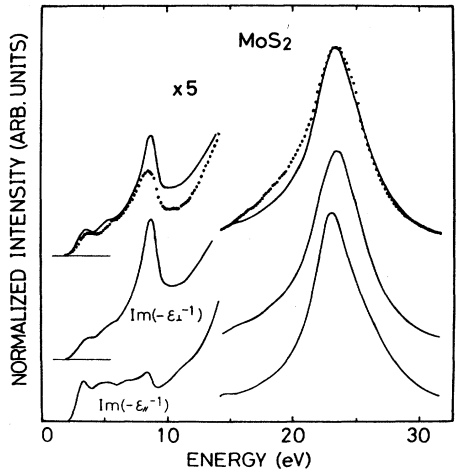

FIG. 8. Comparison between the REELS spectrum of MoS_2 measured at $E_p=2000$ eV (dotted line) and the composite energy-loss function (upper solid line) which is constructed of the energy loss functions perpendicular and parallel to the c axis (middle and bottom solid lines). The mixing ratio is 3.8.

from the TEELS spectra by Zeppenfeld.[24] The solid circles represent the REELS spectrum, which has been measured at $E_p=2000$ eV, while the upper solid line represents the composite energy-loss function, which has been calculated from the perpendicular and parallel components on the basis of the present theory. The mixing ratio is 3.8, which has been evaluated from Eq. (18) by substituting 10 for X_c and setting $\mathrm{Im}(-\epsilon_{\perp}^{-1})/\mathrm{Im}(-\epsilon_{\parallel}^{-1})=1$, because in MoS_2 the magnitude of $\mathrm{Im}(-\epsilon_{\perp}^{-1})$ is nearly equal to that of $\mathrm{Im}(-\epsilon_{\parallel}^{-1})$ at the peak position. For the comparison, all the spectra in Fig. 8 are normalized with maximum intensity. It is found that disagreements arise between the measured spectrum and the composite energy-loss function in the ranges of 8–12 and 16–21 eV. Since the surface loss function exhibits a broad peak around 18 eV, the latter disagreement is attributed to the surface losses. However, at present the cause of the former disagreement is not clear. If θ_c or X_c cannot be well defined, and the upper limit of integral in Eq. (17) is determined by the angular aperture of the CMA, the mixing ratio as well as the intensity depends on energy loss. In this case the mixing ratio is smaller than 3.8, which results in a small correction for the disagreement, but the angular correction for the intensity increases it (see Fig. 4).

Here, it is worth noting that the position of the plasmon peak and its higher-energy tail are in good agreement throughout the spectra. It is known that plasma-frequency or plasma-excitation energy depends on the momentum transfer. In the free-electron approximation it is represented by

$$\hbar\omega_p(q)=\hbar\omega_p(0)+Aq^2\ , \tag{33}$$

where $\omega_p(0)$ is the plasma frequency at $q=0$, and A is a constant, but dependent on a sample. According to Gibbons *et al.*,[25] the width also linearly increases with q^2.

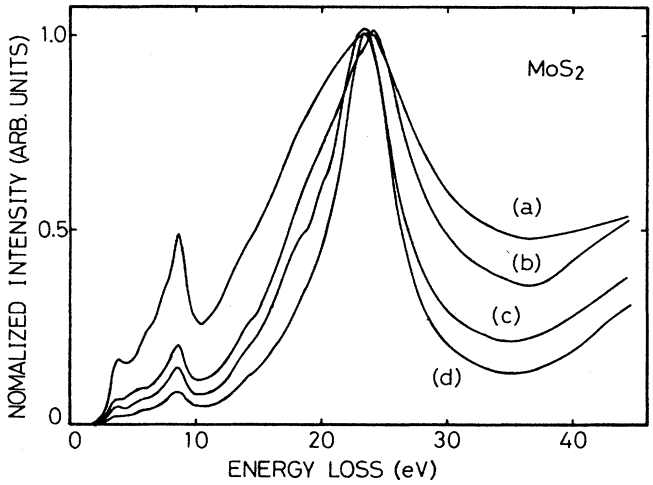

FIG. 9. REELS spectra of MoS_2 measured at various incident energies: (a) 170, (b) 500, (c) 1000, and (d) 2000 eV.

Then, at finite momentum transfer the plasmon peak shifts to higher energy, having larger width compared with that at zero momentum transfer. In the Appendix of the previous paper[19] the present author discussed this in detail for Al and came to the conclusion that most of the momentum transfers affecting the REELS spectrum are less than 0.6 $Å^{-1}$. On the other hand, as can be seen from Fig. 5, the momentum transfer at $\theta=\theta_e$ is less than 0.5 $Å^{-1}$ in most cases, whereas the momentum transfer at $\theta=10\theta_e$ is larger than 1 $Å^{-1}$, except for a low-loss and high-incident-energy region. Summarizing the facts, we may conclude that the REELS spectrum is determined by inelastic scattering in the neighborhood of θ_e, as described in Sec. II. In this case the dipole approximation is valid and the critical inelastic-scattering angle is well defined.

For graphite the perpendicular and parallel energy-loss functions reveal different shapes compared to each other and a plasmon peak appears at quite different energies.[26,27] Furthermore, the magnitude of $\mathrm{Im}(-\epsilon_{\perp}^{-1})$ is 2 times larger than that of $\mathrm{Im}(-\epsilon_{\parallel}^{-1})$. So, the comparison would be more attractive. If the above discussion is right, we may expect the REELS spectrum to be similar to the perpendicular energy-loss function. The measured spectrum is, in fact, quite similar to the perpendicular energy-loss function and almost independent of incident energy. Figures 9 and 10 show the REELS spectra of MoS_2 and graphite at various E_p. It is found that the relative intensities for MoS_2 vary with E_p. This variation would be considered extrinsic; that is, surface effects and background variation due to secondary-electron emission. Later, we will discuss the surface effect on the energy-loss function and on some optical constants.

Next, we will discuss the results of the KK analysis applied to the REELS spectra of MoS_2. Figure 11 shows the real and imaginary parts of the dielectric constants, which are derived from the REELS spectrum measured at $E_p=2000$ eV (thick solid line) and from the composite energy-loss function shown in Fig. 8 (thin solid line). It is found that, although the intensities are slightly different, they exhibit similar structures, the peak and dip positions being almost in agreement. In addition, we find that both ϵ_1 curves cross the horizontal axis at the same energy (see inset). In the free-electron model, without considering the damping of oscillation, the energy corresponds to a plasmon-excitation energy. If the damping exists, the plasmon peak broadens and the crossing energy shifts to lower energy. In the present case the energy value is 22.7 eV, while the plasmon peak is located at 23.4 eV. As discussed below, surface losses affect the energy as if the damping exists.

Figure 12 shows the reflectivity spectra of MoS_2, which are derived from the REELS spectrum at $E_p=2000$ eV

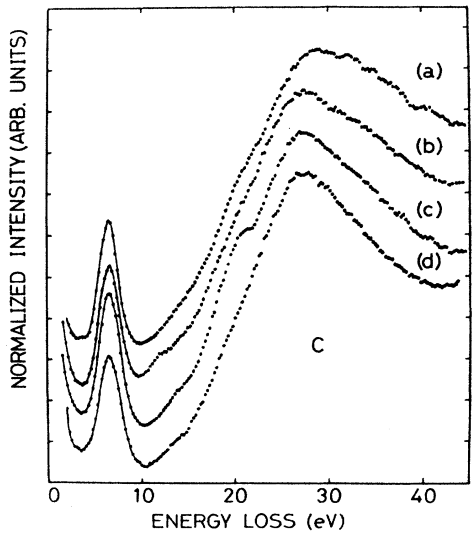

FIG. 10. REELS spectra of graphite measured at various incidence energies: (a) 200, (b) 500, (c) 1000, and (d) 2000 eV.

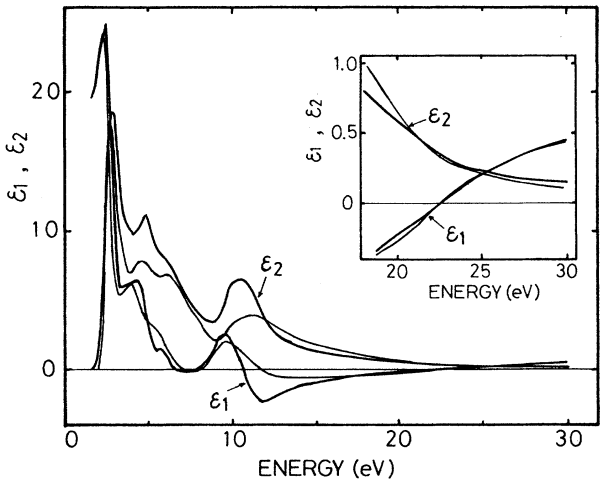

FIG. 11. Real and imaginary parts of the dielectric constant $\epsilon=\epsilon_1+i\epsilon_2$ of MoS_2. The thick solid line represents the dielectric constant derived from the REELS spectrum at $E_p=2000$ eV, while the thin solid line is derived from the composite energy-loss function shown in Fig. 8.

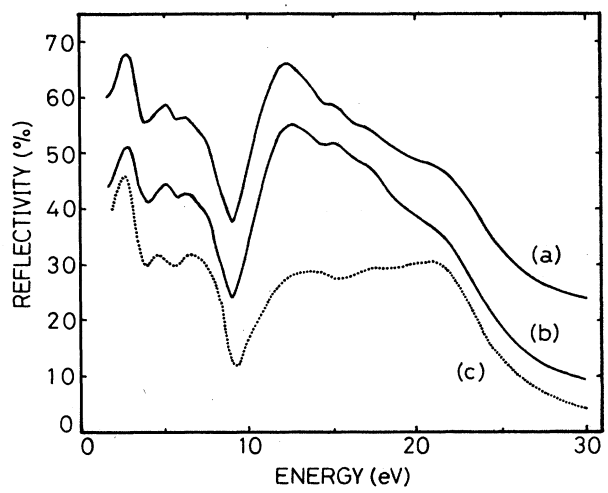

FIG. 12. Comparison between the reflectivity spectra of MoS_2 derived from the REELS spectrum at $E_p=2000$ eV [(a) and (b)] and from the composite energy-loss function shown in Fig. 8 [(c)]. Spectrum (b) is obtained by the KK analysis after subtracting the surface loss function by 20%.

[(a) and (b)] and from the composite energy-loss function [(c)]. In deriving spectrum (b), the KK analysis has been carried out after subtracting the surface loss function by 20%. For comparison, spectra (a) and (b) have been shifted by 20% and 5%, respectively, along the vertical axis. A large disagreement is found between spectra (a) and (c) in the range 10–18 eV, which is not corrected by subtracting the surface losses. This is caused by the introduction of the parameter k into a in implementing the KK analysis. The details will be discussed later. However, in overall appearance they are quite similar to each other and to that of the optical reflectivity spectrum measured by Hughes and Liang,[28] which reveals a large minimum around 9 eV. The interpretation of the spectrum has already been given in another paper.[29] Figure 13 shows the comparison between the refractive-index

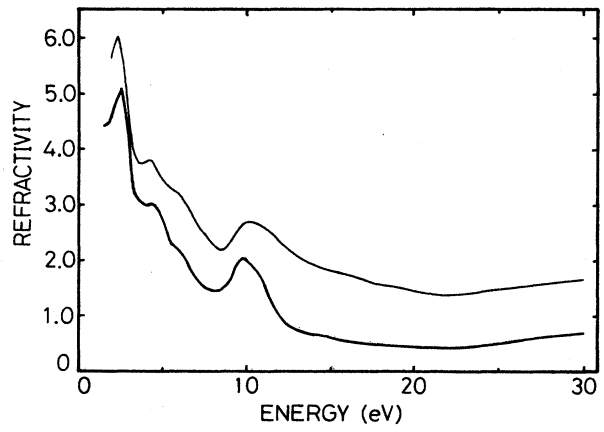

FIG. 13. Comparison between the refractive-index curves of MoS_2 derived from the REELS spectrum at $E_p=2000$ eV (thick solid line) and from the composite energy-loss function shown in Fig. 8 (thin solid line).

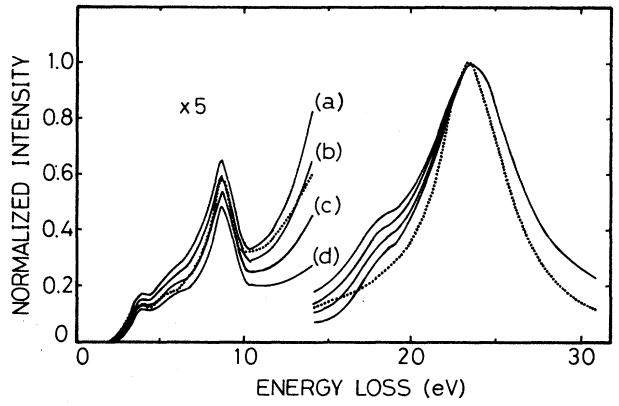

FIG. 14. Comparison between the REELS spectrum of MoS_2 measured at 750 eV [(a)] and the composite energy-loss function shown in Fig. 8 (dotted line). Spectra (b), (c), and (d) are normalized after subtracting the surface loss function by 20%, 40%, and 60%, respectively.

curves. The thin solid line, which represents the refractive-index curve derived from the composite energy-loss function, is shifted by 1.0 along the vertical axis with respect to that of the REELS spectrum. It is found that there is good agreement in shape and intensity.

Figure 14 illustrates the influence of surface losses on the REELS spectrum of MoS_2. Spectrum (a) has been measured at $E_p=750$ eV. Spectra (b), (c), and (d) are normalized after subtracting the surface loss function by 20%, 40%, and 60%, respectively, and the dotted line represents the normalized composite energy-loss function as a reference curve. It is found that the reduction of the surface losses gives rise to the spectrum similar to that at $E_p=2000$ eV, but it cannot be perfectly reconciled with the composite energy-loss function. The disagreement on

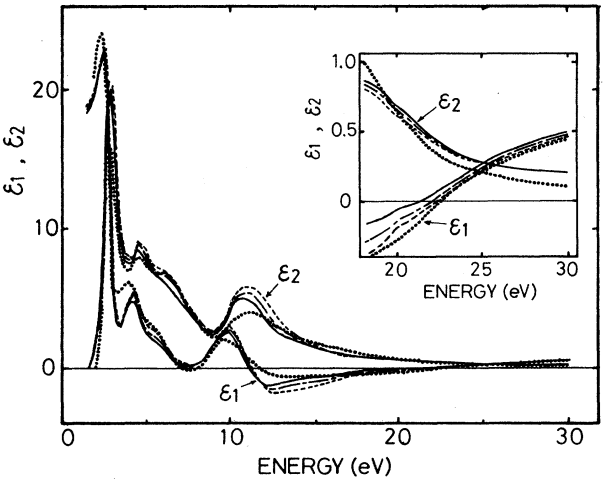

FIG. 15. Comparison between the dielectric constants $\epsilon=\epsilon_1+i\epsilon_2$ of MoS_2 derived from the REELS spectrum at 750 eV (solid line) and from the composite energy-loss function shown in Fig. 8 (dotted line). Long-dashed–short-dashed and dashed lines represent the dielectric constants after subtracting the surface loss function by 20% and 40%, respectively.

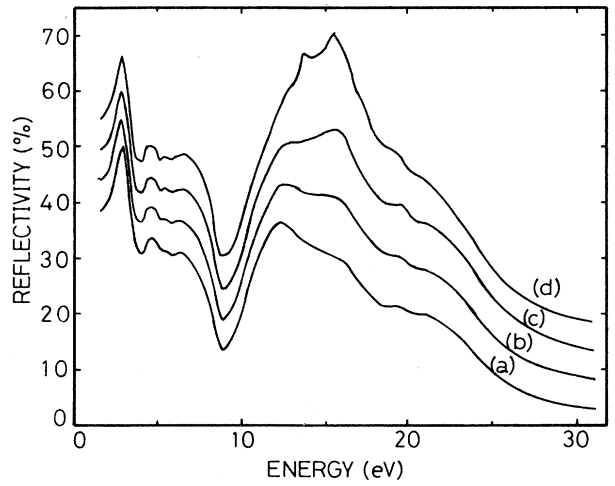

FIG. 16. Reflectivity spectra of MoS_2 derived from the REELS spectrum at 750 eV. Spectra (a), (b), (c), and (d) are obtained by subtracting the surface loss function by 0%, 20%, 40%, and 60%, respectively.

the higher-energy side of the plasmon peak is caused by the incident-energy dependence of the background due to multiple scattering and secondary-electron emission, while the disagreement in the range 10–20 eV is intrinsic, but unknown at present. To investigate the influences of surface losses on the optical constants, we have calculated a dielectric constant, reflectivity, and a refractive index for the respective spectrum shown in Fig. 14. The results are shown in Figs. 15–17. As can be seen from the inset of Fig. 15, the crossing energy of the ϵ_1 curve shifts to higher energy upon subtracting the surface losses, and approaches the value of the composite energy-loss function. This fact suggests that the surface losses behave as if the damping of plasma oscillation increases and gives rise to a broad peak. In comparison with the optical constants derived from the composite energy-loss function, a disagreement is found in the range 10–20 eV, which is apparently increased by subtracting the surface losses. Such a strange variation is caused by the introduction of the parameter k to give a correct $\epsilon_1(0)$ value, because the parameter k itself plays a role in the correction for the surface losses. In fact, in small surface losses an appropriate k value allows one to give reasonable optical constants without subtracting them. The dielectric constant, the reflectivity, and the refractive index are quite similar in total appearance to those from the composite energy-loss function, as well as the energy-loss function perpendicular to the c axis (see Ref. 24). Thus we may conclude that the KK analysis is also valid in REELS to investigate the optical properties and the electronic structures of solids, and that the resulting spectra mainly reveal physical properties perpendicular to the c axis or parallel to the surface.

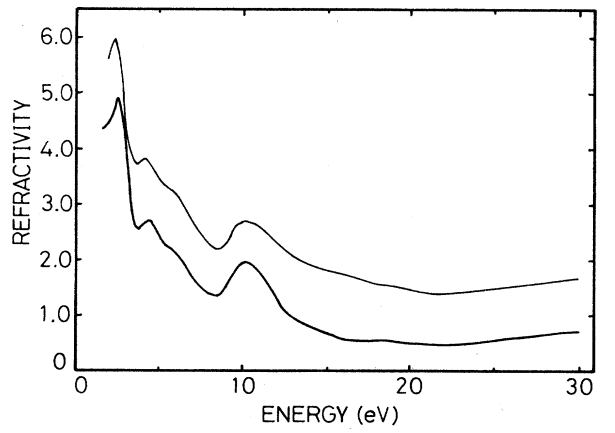

FIG. 17. Comparison between the refractive-index curves of MoS_2 derived from the REELS spectrum at $E_p = 750$ eV by subtracting the surface loss function by 20% (thin solid line) and from the composite energy-loss function shown in Fig. 8 (thick solid line).

V. CONCLUSIONS

In this paper we have discussed the inelastic-scattering process in reflection geometry using a CMA and derived the momentum transfer, the differential cross section, and the mixing ratio of the energy-loss functions perpendicular and parallel to the c axis. The following facts are made clear.

(1) The differential cross section per unit energy and the mixing ratio R are represented as a function of X_c $(=\theta_c/\theta_e)$ and do not depend on energy loss. As a result, the angular correction made in TEELS is not necessary.

(2) A valence-electron energy-loss spectrum is determined mainly by inelastic-scattering events near θ_e $(=\Delta E/2E_p)$.

(3) The dipole approximation is still valid for incident energies higher than 500 eV.

(4) The derived energy-loss function consists approximately of 80% of the perpendicular component and 20% of the parallel component. Then, if the magnitude of the perpendicular energy-loss function is comparable to or more than that of the parallel energy-loss function, the REELS spectrum mainly reveals the energy-loss structures perpendicular to the c axis.

The experimental results have confirmed these facts. The Kramers-Kronig analysis is applied to the REELS spectra of MoS_2 and the results obtained are compared with those of the composite energy-loss function, which is constructed of the energy-loss functions perpendicular and parallel to the c axis at the mixing ratio of 3.8. Surface losses affect the dielectric constant as if the crossing energy of the ϵ_1 curve shifts to lower energy. It is, however, found that the energies are almost in agreement by removing the surface effects. Thus we may conclude that the Kramers-Kronig analysis of a REELS spectrum is valid by removing the background due to multiple scattering and secondary-electron emission and the surface effects by appropriate methods, and further conclude that REELS spectra give valuable information of the optical properties and electronic structures of various solids

in a wide energy range.

In most of the real surfaces, surface atoms are rearranged to reduce the surface energy. In some cases they form a superstructure, resulting in a new electronic structure. In addition, we must take into account the surface states derived from various atomic faults, dangling bonds, and adsorbed foreign atoms and molecules. What has been determined from the REELS spectra are only the energy positions. If we can make direct comparisons between the pulse-counting REELS spectra at low and high incident energies and between the results of the KK analysis, we could derive the surface loss function and surface optical properties from the difference. To do it, however, we need to discuss the effects of the incident-energy dependence of momentum transfer and the differential cross section for inelastic scattering in detail, especially in the energy region where the dipole selection rules are not hold. Furthermore, in a real surface the surface loss function is generally different from that derived from the bulk dielectric function or the energy-loss function because of atomic rearrangement—the theoretical calculation must be carried out individually for each atomic arrangement. However, we believe that in the near future the present study will be extended to real surfaces with the development of the theoretical calculations of surface-electronic structures.

ACKNOWLEDGMENTS

This work is partially supported by a Grant-in-Aid for Scientific Research from the Ministry of Education, Science and Culture of Japan.

[1]C. Colliex, in *Advances in Optical and Electron Microscopy,* edited by V. E. Cosslett and R. Barer (Academic, London, 1984), Vol. 9, p. 65.

[2]R. F. Egerton, *Electron Energy-Loss Spectroscopy in the Electron Microscope* (Plenum, New York, 1986).

[3]J. Daiels, C. V. Festenberg, H. Raether, and K. Zeppenfeld, in Vol. 54 of *Springer Tracts in Modern Physics,* edited by G. Höhler (Springer-Verlag, New York, 1970), p. 78.

[4]H. Raether, in Vol. 88 of *Springer Tracts in Modern Physics,* edited by G. Höhler (Springer-Verlag, New York, 1980).

[5]H. Froitzheim, in *Electron Spectroscopy for Surface Analysis,* Vol. 4 of *Topics in Current Physics,* edited by H. Ibach (Springer-Verlag, New York, 1977), p. 205.

[5]C. J. Powell, Surf. Sci. **44**, 29 (1974).

[7]L. Vriens, J. A. Simpson, and S. R. Mielczarek, Phys. Rev. **165**, 7 (1968).

[8]C. Strasser, G. Rosina, J. A. D. Matthew, and F. P. Netzer, J. Phys. F **15**, 739 (1985).

[9]Y. Ohno, J. Phys. Soc. Jpn. **56**, 3695 (1987).

[10]U. Büchner, Phys. Status Solidi B **81**, 227 (1977); **83**, 493 (1977).

[11]V. E. Henrich, G. Dresselhaus, and H. J. Zeiger, Phys. Rev. **22**, 4764 (1980).

[12]R. Ludeke and L. Esaki, Phys. Rev. Lett. **33**, 653 (1974).

[13]H. Ibach and J. E. Row, Phys. Rev. B **10**, 710 (1974).

[14]R. Ludeke and A. Koma, Phys. Rev. Lett. **34**, 817 (1975).

[15]G. Chiarello, L. S. Caputi, S. Plutino, G. Paolucci, E. Colavita, M. Pecrescenzi, and L. Papagno, Surf. Sci. **146**, 241 (1984).

[16]A. G. Nassiopoulos and J. Cazaux, Surf. Sci. **165**, 203 (1986).

[17]R. D. Leapman, P. Rez, and D. F. Mayers, J. Chem. Phys. **72**, 1232 (1980).

[18]Y. Ohno, Bull. Fac. Gen. Educ. Utsunomiya Univ. **19**, 5 (1986).

[19]Y. Ohno, Phys. Rev. B **36**, 7500 (1987).

[20]C. Kittel, *Introduction to Solid State Physics,* 5th ed. (Wiley, New York, 1976), p. 324.

[21]D. W. Johnson and J. C. H. Spence, J. Phys. D **7**, 771 (1974).

[22]R. D. Leapman and C. R. Swyt, in *Analytical Electron Microscopy,* edited by R. H. Geiss (Freeman, San Francisco, 1981), p. 164.

[23]R. F. Egerton and M. J. Whelan, Philos. Mag. **30**, 739 (1974).

[24]K. Zeppenfeld, Opt. Commun. **1**, 377 (1970).

[25]P. C. Gibbons, S. E. Schnatterly, J. J. Ritsko, and J. R. Fields, Phys. Rev. B **13**, 2451 (1976).

[26]R. Klucher, M. Skibowski, and W. Steinmann, Phys. Status Solidi B **65**, 703 (1974).

[27]H. Venghaus, Phys. Status Solidi B **71**, 609 (1975).

[28]H. P. Hughes and W. Y. Liang, J. Phys. C **10**, 1079 (1977); W. Y. Liang, *ibid.* **4**, L378 (1973).

[29]Y. Ohno, K. Hirama, S. Nakai, C. Sugiura, and S. Okada, Phys. Rev. B **27**, 3811 (1983).